Online needle-tissue interaction model identification for force feedback enhancement in robot-assisted interventional procedures – Supplementary material –

Marco Ferro[1,*]   Claudio Gaz[1]   Michele Anzidei[2]   Marilena Vendittelli[1]

Abstract—**In this document, we report a number of supplementary materials to the main paper. The references here reported are related to the bibliography of the main paper.**

I. Addendum on the rupture detection algorithm

In the presented framework for the needle-tissue interaction force enhancement, we have refined the rupture detection routine by combining the CUSUM algorithm with a force derivative threshold-based condition, so as to obtain a two-step detection process. We observed, in fact, that the adopted constant-frequency covariance matrix reset of the RLS algorithm may alter the statistical characterization of the reconstruction force error signal, since it fosters a higher reactivity of the reconstructed force in tracking the ground truth force measurement. This causes low values of the reconstruction error along the insertion and makes difficult for the CUSUM algorithm to distinguish between *standard* and *abrupt change* cases, thus resulting in possibly missed detections. This force derivative condition is easily formalized through the following decision function $g_{f,k}$:

$$g_{f,k} = \begin{cases} 1, & (f_k - f_{k-1}) > \beta \\ 0, & \text{otherwise} \end{cases} \tag{1}$$

where β is a threshold value chosen experimentally, based on the expected magnitude of the force variations that are observed in the force drop signals due to tissue rupture events.

This criterion is used as a possible pre-condition for the CUSUM detection algorithm as an intermediate detection step. In fact, it specifies a *candidate* force interval in which a tissue detection can likely occur.

In order to facilitate the explanation about how the two criteria are logically connected, we could describe the detection problem of the occurring tissue rupture events through a finite-state machine, as shown in Fig 1. At start, we assume that no tissue ruptures are detected. During the insertion, a tissue rupture is assumed to be detected when the CUSUM algorithm decision function g_k raises to 1 (*Detected rupture* state). Alternatively, if the force derivative-based decision function (1) raises on 1 (i.e., if the force derivative signal has exceeded the threshold β), we fall in a state where we expect that a tissue rupture may likely occur (*Expected rupture* state). At

this stage, we determine a new detected rupture if the CUSUM function g_k raises to 1, or if, despite no CUSUM detections are observed, $g_{f,k}$ falls back to 0 (i.e., on its trailing edge), due to a regularization of the measured force signal. This alternative condition helps to detect possible missing CUSUM-based detections, due to the high reactivity of the reconstruction error resulting from the constant-frequency covariance matrix reset.

After the detection, the system waits for a time $T_{drop,i}$ in order to measure the amount of force drop resulting from the rupture (*Force drop measuring* state), so as to apply the *a posteriori* re-weighting of the covariance matrix and re-estimate the coefficients of the latest traversed layer for compensation (*Force compensation* state). After compensation, the system goes back to the initial state and the detection process is repeated.

II. Remarks on the covariance reset of the RLS routine

Resetting the value of the covariance matrix during the insertion procedure is a technique used in the literature with the purpose of making the RLS algorithm reactive to the changes in the estimating parameters [12,13]. In the present work we use a constant frequency reset mechanism rather than one triggered by the uncertainty lowering below a given threshold, as done in [12,13]. All the experiments that we have conducted show the substantial equivalence of the mechanisms (in both cases either the threshold or the reset frequency value is a parameter to tune). The constant frequency strategy is easier to implement and numerically more robust, hence our choice.

For the considered needle insertion procedures and the adopted interaction model, having a high-frequency reset reveals to be suitable for a proper convergence of the estimating parameters, particularly when handling the considered low-varying position and velocity input signals for the RLS algorithm. In fact, resetting the covariance at a fixed rate has the effect of increasing the excitability of the RLS input signals, making the force estimation more *reactive* in tracking the ground truth force measurements, also when it does not strictly reflect the linearity of the considered model. This behavior has been highlighted in the plots added here in Figs. 10, 11 and 12, where the covariance reset is applied only in correspondence with the detected tissue ruptures, since they represent actual changes in the estimating parameters. The Figures highlight the poor performance of the RLS algorithm in reconstructing properly the force measurements, particularly in the presence of highly nonlinear behaviours, like abrupt force drops.

[1] Dipartimento di Ingegneria Informatica, Automatica e Gestionale, Sapienza Università di Roma, via Ariosto 25, 00185 Roma, Italy. E-mail: {ferro,gaz,vendittelli}@diag.uniroma1.it.
[2] Centro SaNa,Via Peschiera 04011 Aprilia (LT), Italy, E-mail: michele.anzidei@gmail.com.
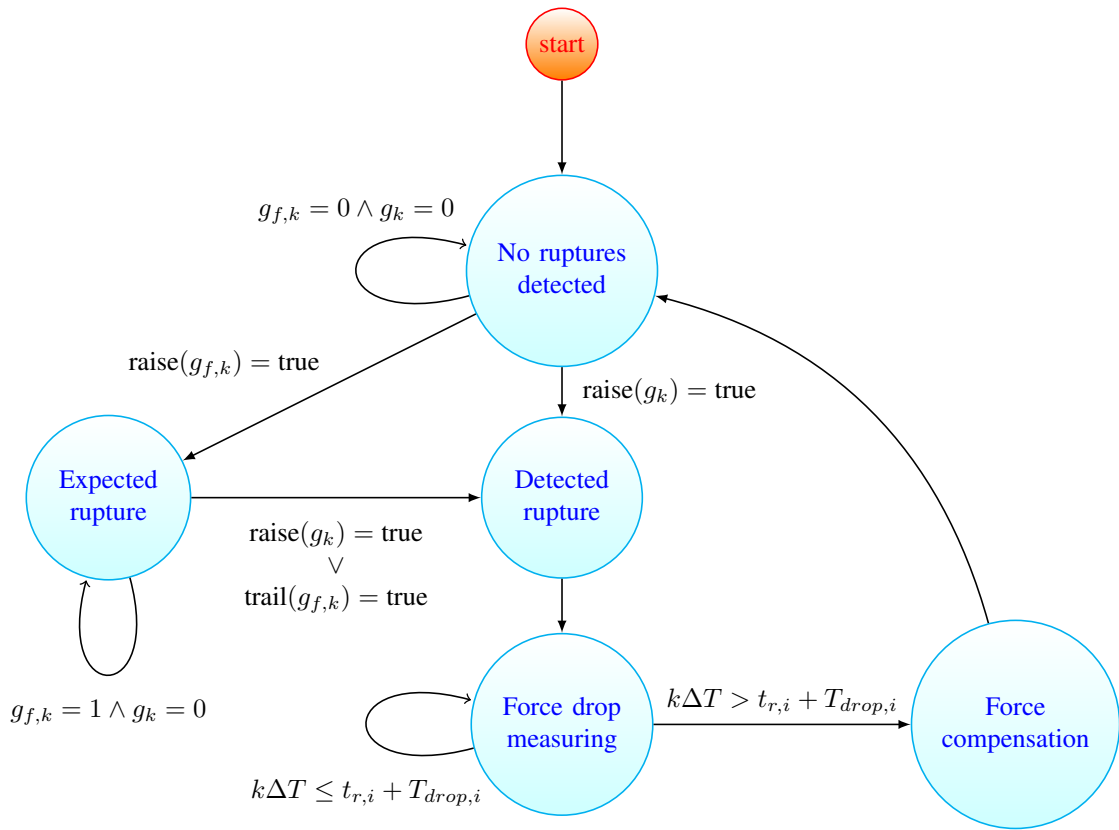* corresponding author.

Fig. 1: Finite state machine describing the algorithm for the detection of tissue rupture events.

Resetting frequently the covariance matrix allows to keep the performance robust against non-linear dynamics in the interaction force and guides the estimation towards more stable and robust values of the coefficients.

This is analogously highlighted in Figs. 13, 14, and 15, where the covariance is applied at the frequency of 40 Hz, while no *a posteriori* reweighting (i.e., Eq. (12) of the main paper) is applied. The performance in the force reconstruction has a significant improvement in this case. However, we also highlight that, since no friction variance reweighting is applied, the estimated friction values are not necessarily physically feasible in the sense previously explained. Indeed, due to the low magnitude of the velocity signal, the reconstructed friction contribution is negligible and does not induce a significant compensation.

III. ADDITIONAL EXPERIMENTAL RESULTS

In this section, we report further experimental results of the presented needle-tissue interaction force enhancement algorithm.

In a first series of experiments, two needle insertions – a first with constant velocity and a second with sinusoidal velocity – have been carried out on each of the three isinglass phantoms (25%, 50% and 70% solution) depicted in Fig. 1 of the main paper, for a total of 6 experiments. Since no latex layer was interposed, we may suppose that the interaction force measured by the F/T sensor is totally due to friction. We estimated the friction coefficients employing the ML model for each experiment both by an offline analysis and by the online

RLS routine, retrieving a total of 12 estimations. In Tab. I of the main manuscript we have reported the average value of those estimations, with variance and corresponding %-wise error. In Figs. 2a and 2b of the present document, we report all the 12 estimated values of friction; in particular, Fig. 2b shows the estimations grouped by isinglass phantom. We can observe that, despite slight lower values when the online routine is used and the needle moves with sinusoidal velocity (as already discussed in the main paper), the friction coefficients are clearly distinguishable between different layers, with no superposition.

Fig. 3a reports the force measured by the real F/T sensor (green line) when the needle traverses a 25% solution isinglass phantom with a constant velocity $v = 2.3$ mm/s; at time $t = 12.5$ s the needle tip exits the layer, so as to leave a constant portion of the shaft inside the phantom. The blue and the red lines represent the enhanced force (discarding the estimated friction terms) obtained using, respectively, the KV and the ML models. It is evident (as well as shown in Sec. V of the main paper) that the ML model is more effective to describe the friction phenomena acting on the needle; in fact, the enhanced force signal offered by the ML model is closer to zero after the layer traversal (when only a constant friction force acts on the needle shaft) with respect to the enhanced force signal returned by means of the KV model. Please note that the compensated force signal after $t = 12.5$ s does not vanish completely (as expected), probably because of the low magnitude of the involved interaction force (whose range is 0.5 N). Fig. 3b reports the estimated elastic (upper panel),
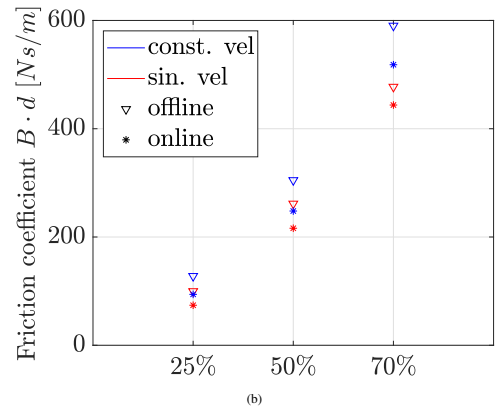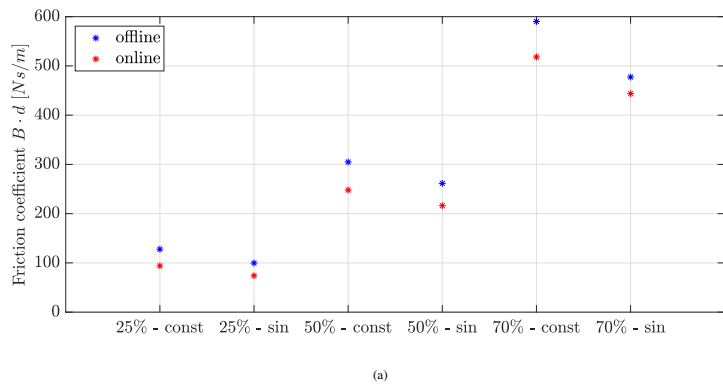
Fig. 2: (a-b) Aggregated comparison of estimated friction values in insertions through single-layer phantoms with different solution.

friction (middle panel) and cumulative friction (bottom panel) coefficients during the experiment.

Fig. 4a shows the results obtained when the needle is inserted in a 50% solution isinglass phantom with a constant velocity $v = 2.3$ mm/s. The interaction force, measured by the real F/T sensor, is reported in green. In this experiment we may appreciate again a more effective interaction force enhancement after the needle tip traverses the phantom completely (this occurs at $t = 17$ s) when the ML model is used (red line) in place of the KV model (blue line). Fig. 4b reports the estimated elastic (upper panel), friction (middle panel) and cumulative friction (bottom panel) coefficients during the experiment.

Figs. 5a and 6a report the results of two different experiments using, respectively, a 25% and a 50% solution isinglass phantom; the needle is moved with a sinusoidal velocity. The green lines represent the interaction force signal measured by a real F/T sensor, while the blue and the red lines are, respectively, the enhanced force signal using the KV and the ML models. In Fig. 5a we can observe that the KV model overcompensates the friction component of the interaction force, probably because of a poor estimation of this term. Figs. 5b and 6b report the estimated elastic (upper panel), friction (middle panel) and cumulative friction (bottom panel) coefficients associated to the two experiments.

A further experiment has been carried out on the stack of three layers (see Fig. 3a of the main paper), with the middle layer enveloped by a latex glove. The needle is moved with a sinusoidal velocity. The results of this experiment are reported in Fig. 7a: the green line represents the force measured by the real F/T sensor, while the blue and the red lines represent, respectively, the enhanced force when the KV and the ML models are used. Comparing Fig. 7a with Fig. 12 of the main paper (same phantom stack but constant needle velocity), we can observe that the three layer ruptures are correctly detected (vertical black continuous lines) even when the needle velocity is not constant. Fig. 7b reports the estimated elastic (upper panel), friction (middle panel) and cumulative friction (bottom panel) coefficients during the experiment.

Fig. 8a reports the results of a needle insertion experiment using as a phantom a real bovine liver. The insertion velocity is constant, making this experiment equivalent to the one whose

results are reported in Fig. 13 of the main paper. Differently from the corresponding experiment of the main paper, here the interaction force is measured by a real F/T sensor. Comparing Fig. 8a of this document with Fig. 13 of the main paper, we can observe that the two layer ruptures (vertical continuous black lines) are correctly detected in both cases: this proves once again the effectiveness of the use of the proposed virtual F/T sensor presented in Sec. III of the main paper. Furthermore, even in this case the use of the ML model (red line) makes the compensated force more effective in rendering the elastic component of the interaction force with respect the use of the KV model (blue line). Fig. 8b reports the estimated elastic (upper panel), friction (middle panel) and cumulative friction (bottom panel) coefficients during the experiment.

Finally, one last experiment has been carried out on the medical abdominal phantom shown in Fig. 7 of the main paper. The needle insertion velocity is sinusoidal, so as to have the same operative conditions of the experiment whose results are reported in Fig. 14 of the main paper. Fig. 9a reports the force measured during the insertion by a real F/T sensor (green line), while the blue and the red lines represent the compensated force using, respectively, the KV and the ML model. Comparing Fig. 9a of the present document with Fig. 14 of the main paper, we can notice that the two layer ruptures (vertical continuous black lines) are correctly detected both using the real or the virtual F/T sensor.

IV. WEIGHTING THE COVARIANCE MATRIX IN THE RLS ALGORITHM

In this section, we will detail the re-weighting procedure mentioned in Sec. II-C of the main paper. This procedure is carried out to overcome possible identifiability issues due to non-exciting motions performed by the needle. For instance, if the needle is moved according to a constant velocity, it is not possible to discriminate between the elastic and the viscous component of the interaction force. This is evident observing Eqs. (4)-(6) of the main paper: indeed, for a given layer i, in the presence of a constant needle velocity $\bar{v}$ we have that two columns of the regressor $\mathbf{\Phi}$ are linearly dependent, thus invalidating an offline identification procedure. Nevertheless, even an online procedure, such as the one adopted in this work, based on the RLS algorithm, is heavily affected by this

issue. Furthermore, we noted that even time-varying motions may cause the same identifiability problem, if they are not particularly exciting. This class of motions are however very common in normal operative conditions.

Therefore we propose a method to exploit additional information offered by the layer rupture events, to assign different weights to the RLS covariance matrix and thus enhance the identification algorithm even in the presence of not particularly exciting motions.

Consider a generic needle-tissue interaction model formalized as a combination of elastic and friction contributions

$$
\begin{aligned}
f(t) &= f_K(t) + f_B(t) = \\
&= K\varphi_K + B\varphi_B = \\
&= \boldsymbol{\varphi}^T\boldsymbol{\theta}
\end{aligned}
\tag{2}
$$

where $\boldsymbol{\varphi} = [\varphi_K, \varphi_B]^T$ is the vector of elastic and friction contributions, while $\boldsymbol{\theta} = [K, B]^T$ is the vector of the corresponding coefficients.

Eq. (2) can be detailed by the Kelvin-Voigt (KV) model, with:

$$
\boldsymbol{\varphi}(t) = \begin{bmatrix} \varphi_K \\ \varphi_B \end{bmatrix}\begin{bmatrix} \Delta z(t) \\ v(t) \end{bmatrix},
\tag{3}
$$

where $\Delta z(t)$ is the needle tip relative depth with respect to the initial position of the current layer L_i, and $v(t)$ is velocity during the insertion in the target tissue. With reference to the main paper, we formalized the *multi-layer* (ML) model by expressing a direct dependence of the friction component on the needle tip position $\Delta z(t)$, and assuming a third contribution collecting the cumulative friction of the previously traversed tissue layers:

$$
\boldsymbol{\varphi} = \begin{bmatrix} \varphi_K(t) \\ \varphi_B(t) \end{bmatrix} = \begin{bmatrix} \Delta z(t) \\ \Delta z(t)v(t) \end{bmatrix}.
\tag{4}
$$

In the formulation above, we ignored the third contribution due to the cumulative friction term, as reported in the main paper, since it is not informative for the following analysis.

Assuming that a measurement of the interaction force is available (e.g., from a F/T sensor or a residual-based reconstruction – see Sec. III of the main paper), and chosen one of the models (3) or (4), we estimate the unknown dynamic coefficients through the Recursive Least Square (RLS) algorithm at a given time k:

$$
\begin{aligned}
\hat{\boldsymbol{\theta}}_k &= \hat{\boldsymbol{\theta}}_{k-1} + \frac{\hat{\boldsymbol{\Psi}}_{k-1}\boldsymbol{\varphi}_k e_k}{\lambda_k + \boldsymbol{\varphi}^T\hat{\boldsymbol{\Psi}}_{k-1}\boldsymbol{\varphi}_k} \\
\boldsymbol{\Psi}_k &= \boldsymbol{\Psi}_{k-1} - \frac{\boldsymbol{\Psi}_{k-1}\boldsymbol{\varphi}_k\boldsymbol{\varphi}_k^T\boldsymbol{\Psi}_{k-1}}{\lambda_k + \boldsymbol{\varphi}^T\boldsymbol{\Psi}_{k-1}\boldsymbol{\varphi}_k}
\end{aligned}
\tag{5}
$$

where $\boldsymbol{\Psi}$ is the covariance matrix of the associated estimation $\hat{\boldsymbol{\theta}}$, $\boldsymbol{\varphi}$ is the input vector, $e_k = f_k - \hat{\boldsymbol{\theta}}_{k-1}\boldsymbol{\varphi}$ is the force reconstruction error and λ_k (by default = 1) is the forgetting factor. The RLS algorithm is shown to be strongly dependent on a proper initialization of the covariance matrix $\boldsymbol{\Psi}_0$ at time 0. A typical approximated initialization is given by

$$
\boldsymbol{\Psi}_0 = \begin{bmatrix} \sigma_0^2 & 0 \\ 0 & \sigma_0^2 \end{bmatrix} = \sigma_0^2\boldsymbol{I}_3,
\tag{6}
$$

with $\sigma_0 \in \mathbb{R}$. We can generalize (6) and consider different values for the corresponding coefficients to be estimated, as:

$$
\boldsymbol{\Psi}_0' = \begin{bmatrix} \sigma_K^2 & 0 \\ 0 & \sigma_B^2 \end{bmatrix}.
\tag{7}
$$

Without loss of generalization, In particular, matrix $\boldsymbol{\Psi}_0'$ can be considered as a *weighted* version of $\boldsymbol{\Psi}_0$, as we can write:

$$
\boldsymbol{\Psi}_0' = \boldsymbol{W}\boldsymbol{\Psi}_0 = \begin{bmatrix} w_K^2 & 0 \\ 0 & w_B^2 \end{bmatrix}\begin{bmatrix} \sigma_0^2 & 0 \\ 0 & \sigma_0^2 \end{bmatrix}
\tag{8}
$$

such that $\sigma_K^2 = w_K^2\sigma_0^2$ and $\sigma_B^2 = w_B^2\sigma_0^2$. Alternatively, Eq. (8) can be also written as

$$
\boldsymbol{\Psi}_0' = \boldsymbol{W}\boldsymbol{\Psi}_0 = \boldsymbol{\Lambda}\boldsymbol{\Psi}_0\boldsymbol{\Lambda}^T = \boldsymbol{\Lambda}\boldsymbol{\Psi}_0\boldsymbol{\Lambda},
\tag{9}
$$

being

$$
\boldsymbol{\Lambda} = \begin{bmatrix} w_K & 0 \\ 0 & w_B \end{bmatrix}
\tag{10}
$$

Based on (9), replacing $\boldsymbol{\Psi}$ with $\boldsymbol{\Psi}'$ in (5), we get

$$
\begin{cases}
\hat{\boldsymbol{\theta}}_k = \hat{\boldsymbol{\theta}}_{k-1} + \dfrac{\boldsymbol{\Lambda}\boldsymbol{\Psi}_{k-1}\boldsymbol{\Lambda}\boldsymbol{\varphi}_k e_k}{\lambda_k + \boldsymbol{\varphi}^T\boldsymbol{\Lambda}\boldsymbol{\Psi}_{k-1}\boldsymbol{\Lambda}\boldsymbol{\varphi}_k} \\
\boldsymbol{\Psi}_k = \boldsymbol{\Lambda}\boldsymbol{\Psi}_{k-1}\boldsymbol{\Lambda} - \dfrac{\boldsymbol{\Lambda}\boldsymbol{\Psi}_{k-1}\boldsymbol{\Lambda}\boldsymbol{\varphi}_k\boldsymbol{\varphi}_k^T\boldsymbol{\Lambda}\boldsymbol{\Psi}_{k-1}\boldsymbol{\Lambda}}{\lambda_k + \boldsymbol{\varphi}^T\boldsymbol{\Lambda}\boldsymbol{\Psi}_{k-1}\boldsymbol{\Lambda}\boldsymbol{\varphi}_k}
\end{cases} =
$$

$$
\begin{cases}
\hat{\boldsymbol{\theta}}_k = \hat{\boldsymbol{\theta}}_{k-1} + \boldsymbol{\Lambda}\dfrac{\boldsymbol{\Psi}_{k-1}\boldsymbol{\varphi}_k' e_k}{\lambda_k + \boldsymbol{\varphi}_k'^T\boldsymbol{\Psi}_{k-1}\boldsymbol{\varphi}_k'} \\
\boldsymbol{\Psi}_k = \boldsymbol{\Lambda}\left(\boldsymbol{\Psi}_{k-1} - \dfrac{\boldsymbol{\Psi}_{k-1}\boldsymbol{\varphi}_k'\boldsymbol{\varphi}_k'^T\boldsymbol{\Psi}_{k-1}}{\lambda_k + \boldsymbol{\varphi}_k'^T\boldsymbol{\Psi}_{k-1}\boldsymbol{\varphi}_k'}\right)\boldsymbol{\Lambda}
\end{cases} =
\tag{11}
$$

where we set

$$
\boldsymbol{\varphi}_k' = \boldsymbol{\Lambda}\boldsymbol{\varphi}_k
\tag{12}
$$

In our experimental setup, we considered in a first stage a linear trajectory with constant velocity, i.e.,

$$
\begin{aligned}
z(t) &= \frac{t}{T} \\
v(t) &= \frac{\partial z(t)}{\partial t} = \frac{1}{T} = \bar{v} = const.
\end{aligned}
\tag{13}
$$

Relationships above show that a given weighting of the covariance matrix through a matrix $\boldsymbol{W} = \boldsymbol{\Lambda}\boldsymbol{\Lambda}^T$ (see Eq. 9) affects the RLS update step and in particular the input vector $\boldsymbol{\varphi}$ through Eq. (12). Within this perspective, the normalization of the damping coefficient in the ML model by the depth d of the current layer can be actually seen as a weight on the input vector

$$
\boldsymbol{\varphi}' = \boldsymbol{\Lambda}_d\boldsymbol{\varphi} = \begin{bmatrix} 1 & 0 \\ 0 & \frac{1}{d} \end{bmatrix}\begin{bmatrix} \Delta z(t) \\ \Delta z(t)v(t) \end{bmatrix}.
\tag{14}
$$

Therefore, applying the following weighting matrix $\boldsymbol{W}_d$

$$
\boldsymbol{W}_d = \boldsymbol{\Lambda}_d\boldsymbol{\Lambda}_d^T\begin{bmatrix} 1 & 0 \\ 0 & \frac{1}{d^2} \end{bmatrix}.
\tag{15}
$$

is equivalent at normalizing the input vector $\boldsymbol{\varphi}$ by the depth value d. Furthermore, we also apply an additional weight $\boldsymbol{W}_h$

on the covariance matrix $\boldsymbol{\Psi}$ in order to make the input signals $z(t)$ and $v(t)$ homogeneous in magnitude:

$$\boldsymbol{W}_h = \begin{bmatrix} 1 & 0 \\ 0 & \dfrac{d^2}{v^2} \end{bmatrix} \tag{16}$$

Therefore, combining the weight matrices $\boldsymbol{W}_h$ and $\boldsymbol{W}_d$, we get a final weight matrix $\boldsymbol{W}$:

$$\boldsymbol{W} = \boldsymbol{W}_h \boldsymbol{W}_d = \begin{bmatrix} 1 & 0 \\ 0 & \dfrac{d^2}{v^2} \end{bmatrix} \begin{bmatrix} 1 & 0 \\ 0 & \dfrac{1}{d^2} \end{bmatrix} = \begin{bmatrix} 1 & 0 \\ 0 & \dfrac{1}{v^2} \end{bmatrix}, \tag{17}$$

that explains the expression of the re-scaling of σ_B in Eq. (12) of the main paper.
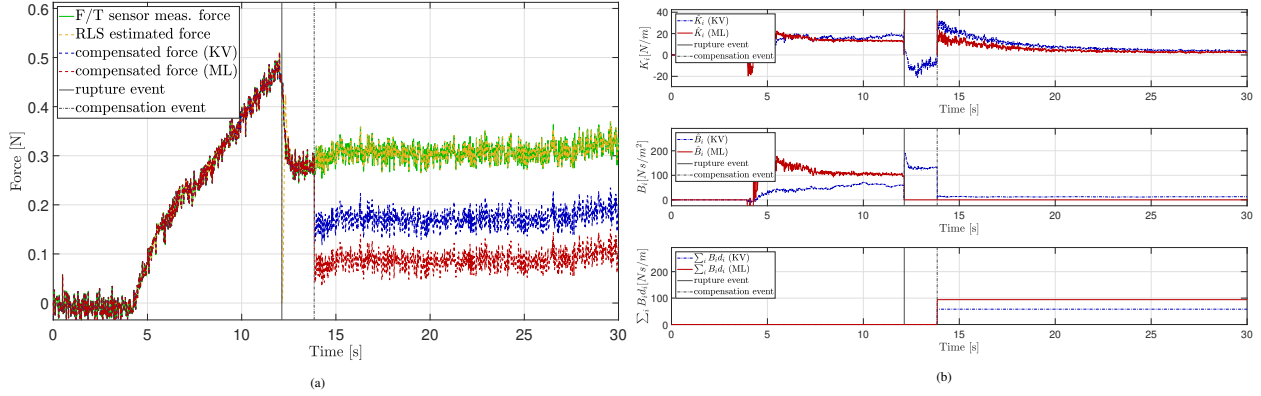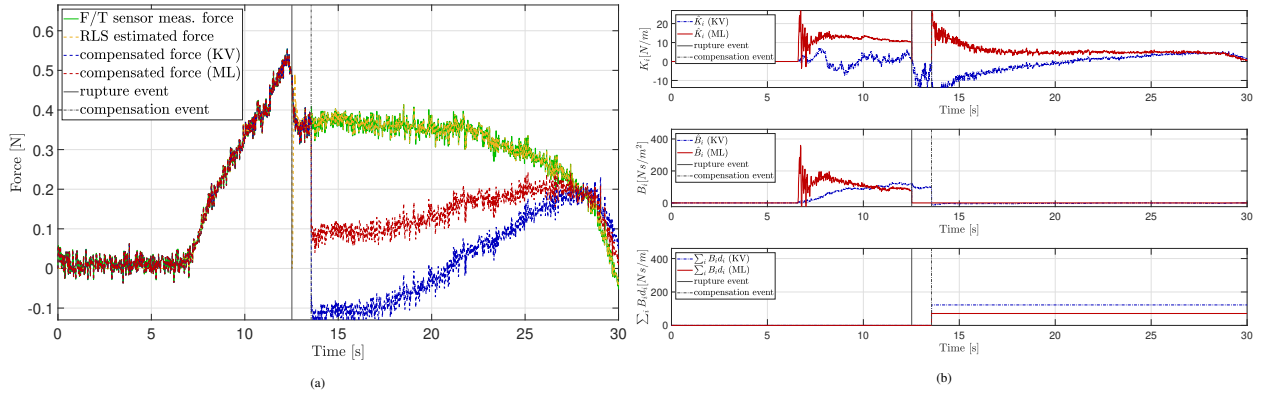
Fig. 3: Experimental results of the friction compensation algorithm on the 25% solution gel phantom, with unknown layer depth. The needle insertion occurs with a constant velocity. (a) Measured (green), predicted (yellow) and compensated forces using the KV (blue line) and the ML (red line) models. With vertical black lines are highlighted the rupture detection time t_r (continuous line) and the compensation time $t_r + T_{drop}$ (dashed line). (b) Estimation of the elastic (upper panel), local friction (middle panel) and cumulative friction (bottom panel) parameters for the presented experiment.
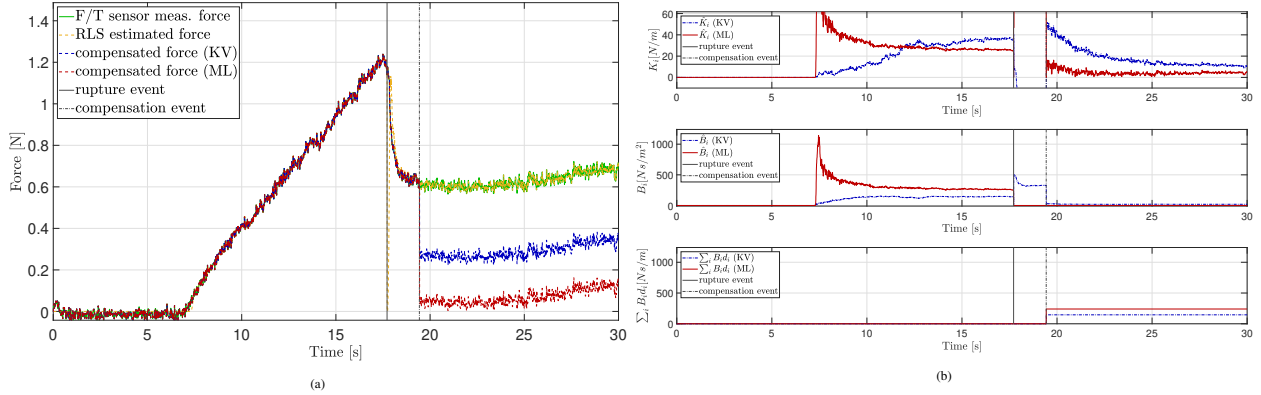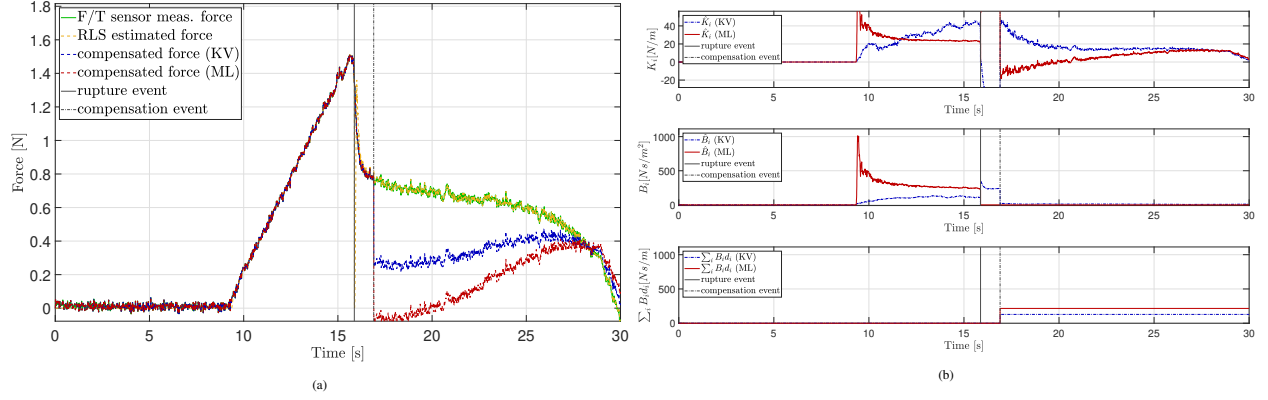

Fig. 4: Experimental results of the friction compensation algorithm on the 50% solution gel phantom, with unknown layer depth. The needle insertion occurs with a constant velocity. (a) Measured (green), predicted (yellow) and compensated forces using the KV (blue line) and the ML (red line) models. With vertical black lines are highlighted the rupture detection time t_r (continuous line) and the compensation time $t_r + T_{drop}$ (dashed line). (b) Estimation of the elastic (upper panel), local friction (middle panel) and cumulative friction (bottom panel) parameters for the presented experiment.
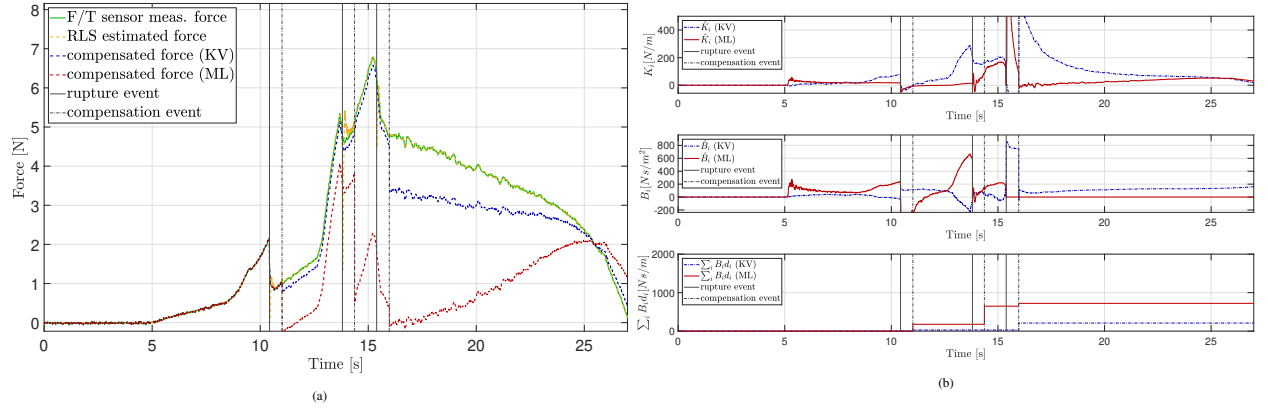

Fig. 5: Experimental results of the friction compensation algorithm on the 25% solution gel phantom, with unknown layer depth. The needle insertion occurs with a sinusoidal velocity. (a) Measured (green), predicted (yellow) and compensated forces using the KV (blue line) and the ML (red line) models. With vertical black lines are highlighted the rupture detection time t_r (continuous line) and the compensation time $t_r + T_{drop}$ (dashed line). (b) Estimation of the elastic (upper panel), local friction (middle panel) and cumulative friction (bottom panel) parameters for the presented experiment.

Fig. 6: Experimental results of the friction compensation algorithm on the 50% solution gel phantom, with unknown layer depth. The needle insertion occurs with a sinusoidal velocity. (a) Measured (green), predicted (yellow) and compensated forces using the KV (blue line) and the ML (red line) models. With vertical black lines are highlighted the rupture detection time t_r (continuous line) and the compensation time $t_r + T_{drop}$ (dashed line). (b) Estimation of the elastic (upper panel), local friction (middle panel) and cumulative friction (bottom panel) parameters for the presented experiment.

Fig. 7: Experimental results of the friction compensation algorithm on the stack of three gel phantom (from top to bottom: 20%, 50% and 70% solution), with unknown layer depth and with the middle layer enveloped by a latex glove. The needle insertion occurs with a sinusoidal velocity. (a) Measured (green), predicted (yellow) and compensated forces using the KV (blue line) and the ML (red line) models. With vertical black lines are highlighted the rupture detection time t_r (continuous line) and the compensation time $t_r + T_{drop}$ (dashed line). (b) Estimation of the elastic (upper panel), local friction (middle panel) and cumulative friction (bottom panel) parameters for the presented experiment.
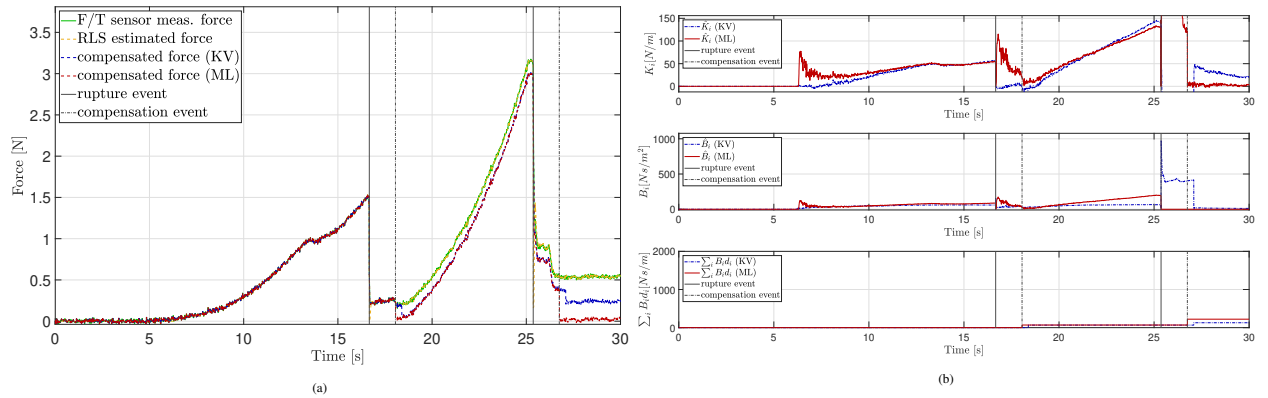

Fig. 8: Experimental results of the friction compensation algorithm on the bovine liver. The needle insertion occurs with a constant velocity. (a) Measured (green), predicted (yellow) and compensated forces using the KV (blue line) and the ML (red line) models. With vertical black lines are highlighted the rupture detection time t_r (continuous line) and the compensation time $t_r + T_{drop}$ (dashed line). (b) Estimation of the elastic (upper panel), local friction (middle panel) and cumulative friction (bottom panel) parameters for the presented experiment.
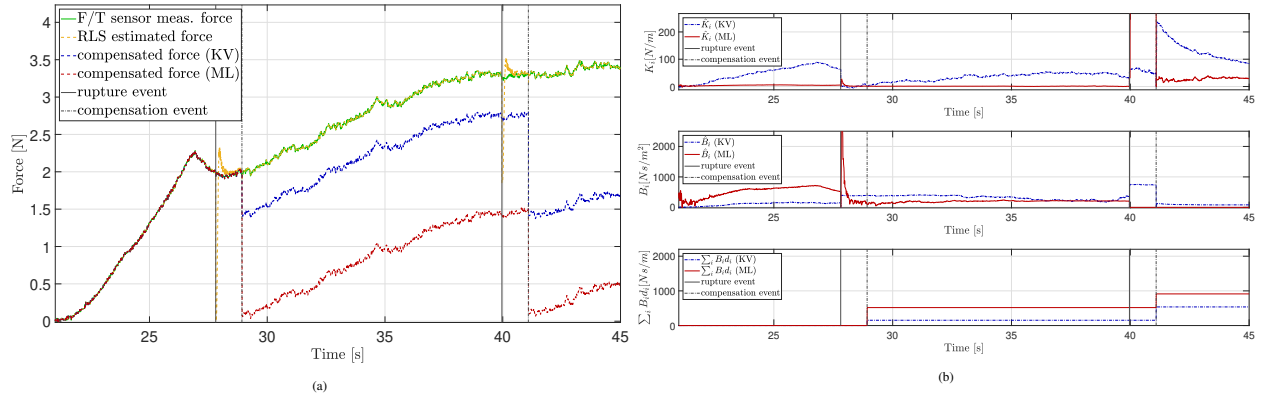
Fig. 9: Experimental results of the friction compensation algorithm on the abdominal phantom. The needle insertion occurs with a sinusoidal velocity. (a) Measured (green), predicted (yellow) and compensated forces using the KV (blue line) and the ML (red line) models. With vertical black lines are highlighted the rupture detection time t_r (continuous line) and the compensation time $t_r + T_{drop}$ (dashed line). (b) Estimation of the elastic (upper panel), local friction (middle panel) and cumulative friction (bottom panel) parameters for the presented experiment.
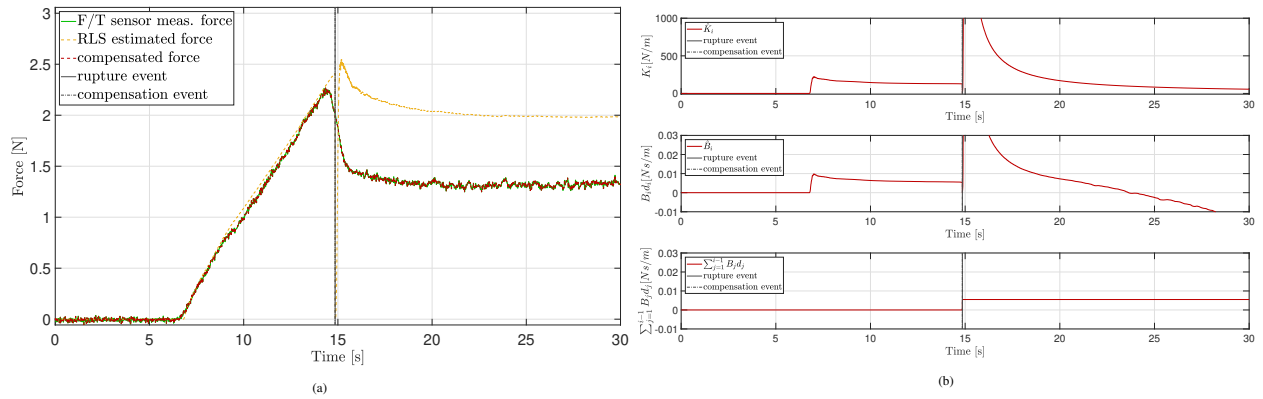
Fig. 10: Performance of the RLS reconstructed force (a) and related estimated coefficients (b) when the covariance matrix is reset only at the detected rupture events, over a single-layer 70% isinglass phantom with constant insertion velocity.
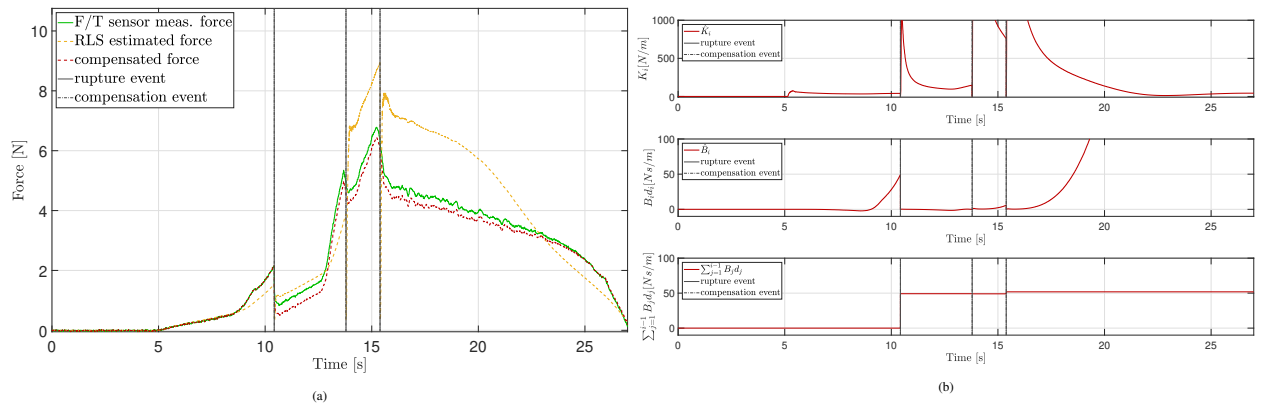

Fig. 11: Performance of the RLS reconstructed force (a) and related estimated coefficients (b) when the covariance matrix is reset only at the detected rupture events, over a multi-layer isinglass phantom with sinusoidal insertion velocity.
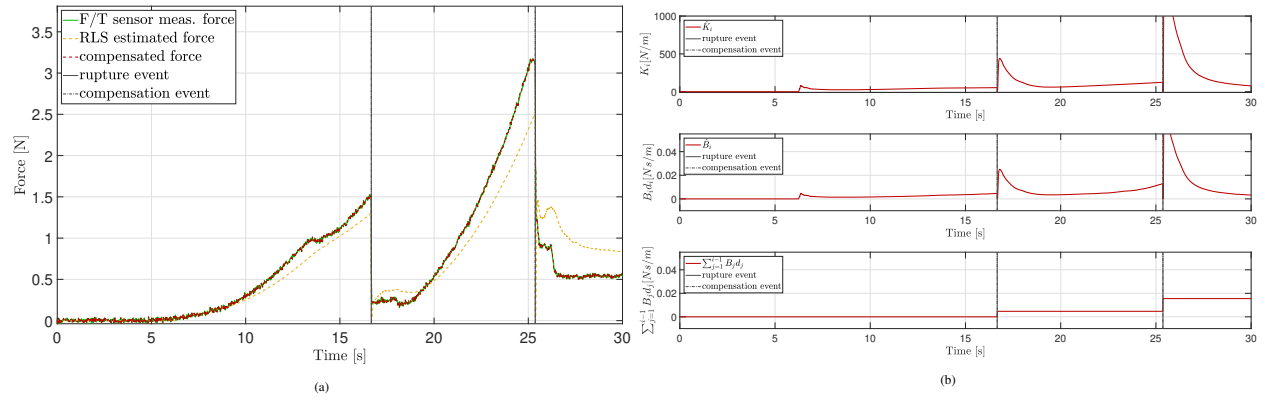
Fig. 12: Performance of the RLS reconstructed force (a) and related estimated coefficients (b) when the covariance matrix is reset only at the detected rupture events, over a bovine liver target with constant insertion velocity.
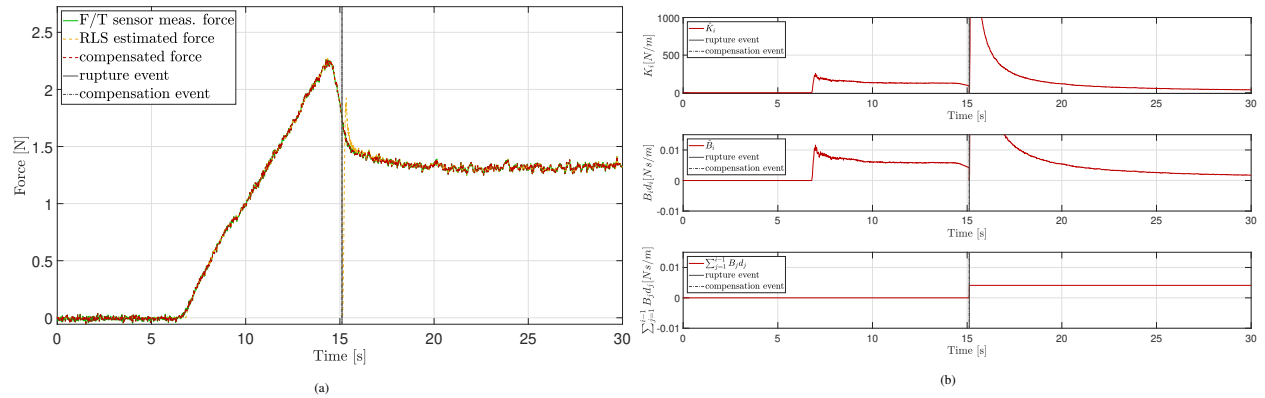

Fig. 13: Performance of the RLS reconstructed force (a) and related estimated coefficients (b) with constant-frequencty covariance reset and no *a posteriori* covariance re-weighting, over a single-layer 70% isinglass phantom with sinusoidal insertion velocity.
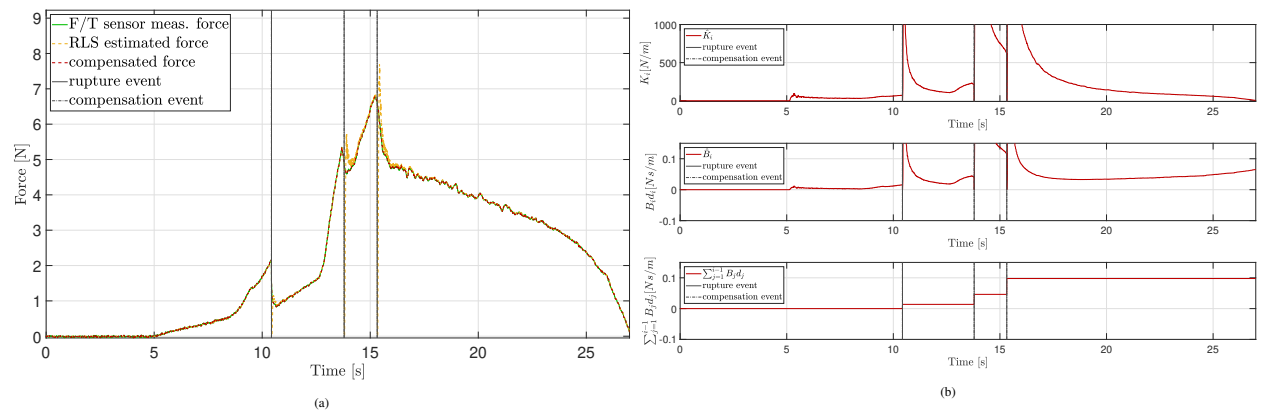

Fig. 14: Performance of the RLS reconstructed force (a) and related estimated coefficients (b) with constant-frequencty covariance reset and no *a posteriori* covariance re-weighting, over a multi-layer isinglass phantom with sinusoidal insertion velocity.
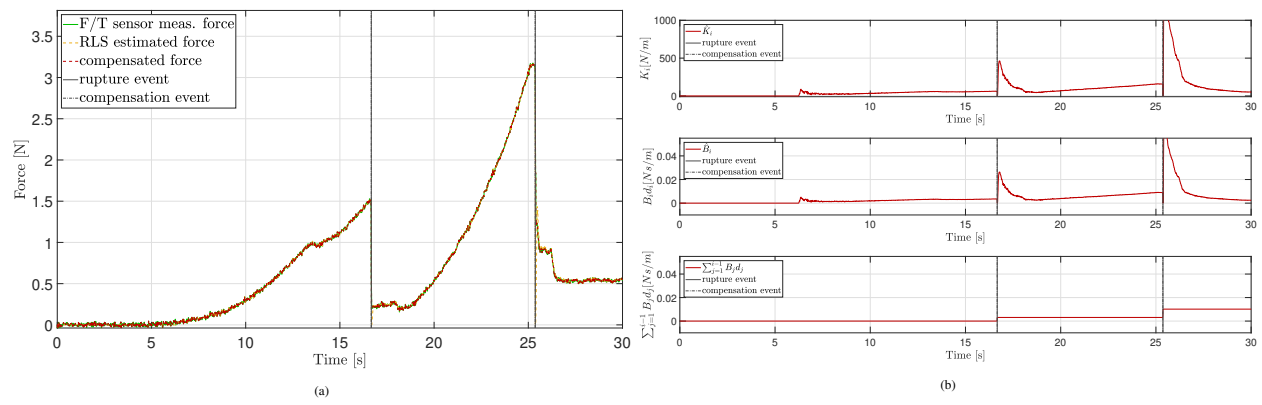
(a)

(b)

Fig. 15: Performance of the RLS reconstructed force (a) and related estimated coefficients (b) with constant-frequencty covariance reset and no *a posteriori* covariance re-weighting, over a bovine liver target with constant insertion velocity.